




# Development of InAs/InAsSb Type II Strained-Layer Superlattice Unipolar Barrier Infrared Detectors

DAVID Z. TING <sup>1,3</sup> ALEXANDER SOIBEL,<sup>1</sup>  
AREZOU KHOSHAKHLAGH,<sup>1</sup> SAM A. KEO,<sup>1</sup> SIR B. RAFOL,<sup>1</sup>  
LINDA HÖGLUND,<sup>1,2</sup> EDWARD M. LUONG,<sup>1</sup> ANITA M. FISHER,<sup>1</sup>  
CORY J. HILL,<sup>1</sup> and SARATH D. GUNAPALA<sup>1</sup>

1.—NASA Jet Propulsion Laboratory, California Institute of Technology, M/S 302-231, 4800 Oak Grove Drive, Pasadena, CA 91109-8099, USA. 2.—*Present address:* IRnova AB, Kista, Sweden. 3.—e-mail: David.Z.Ting@jpl.nasa.gov

We recently reported mid-wavelength infrared (MWIR) InAs/InAsSb type II strained-layer superlattice (T2SLS) unipolar barrier detectors and focal-plane arrays with significantly higher operating temperature than InSb. Herein, we document the development leading to the MWIR InAs/InAsSb T2SLS detectors at the NASA Jet Propulsion Laboratory. We also briefly compare the InAs/InAsSb T2SLS with some other approaches.

**Key words:** Infrared detector, unipolar barrier, *nBn*, mid-wavelength infrared, type II superlattice

## INTRODUCTION

Traditionally, the two main mid-wavelength infrared (MWIR) focal-plane array (FPA) technologies are based on InSb and HgCdTe (MCT) infrared absorbers, each with its own distinct advantages. InSb dominates the MWIR FPA market in volume because of the superior manufacturability afforded by the robustness of III–V semiconductors. On the other hand, the II–VI semiconductor-based MCT can achieve much lower dark current and/or higher operating temperature, and is the detector of choice for more demanding applications. Recently, we reported device and FPA results on a mid-wavelength InAs/InAsSb type II strained-layer superlattice (T2SLS) high-operating-temperature (HOT) unipolar barrier infrared detector (BIRD).<sup>1</sup> At 160 K, the 50% cutoff wavelength is 5.42  $\mu\text{m}$ , and the FPA exhibits a 300-K background,  $f/2$  aperture mean noise-equivalent differential temperature (NEDT) of 18.7 mK ( $\sigma = 9.2$  mK), with NEDT operability of 99.7% and  $D^* = 1 \times 10^{11}$  cm Hz<sup>1/2</sup>/W.<sup>2</sup> The InAs/InAsSb T2SLS HOT-BIRD FPA retains

the same III–V semiconductor manufacturability benefits of InSb, but operates at significantly higher temperatures. This result demonstrates that type II superlattices can be highly competitive with respect to a major incumbent infrared detector technology (InSb). We document herein the development leading to the InAs/InAsSb T2SLS detector at the NASA Jet Propulsion Laboratory (JPL).

## DEVELOPMENT OF InAs/InAsSb/InSb-BASED MID-WAVELENGTH INFRARED DETECTORS

The performance of III–V semiconductor-based infrared detectors has been hampered by relatively short minority-carrier lifetime and the lack of effective surface passivation, leading to generation–recombination (G–R) and surface leakage dark currents, respectively. The 2006 *nBn* paper by Maimon and Wicks<sup>3</sup> showed that an electron unipolar barrier can be used in many instances to suppress these undesired dark currents. The initial *nBn* devices used either InAs absorber grown on an InAs substrate or lattice-matched InAsSb alloy grown on a GaSb substrate, with cutoff wavelength of  $\sim 3.2$   $\mu\text{m}$  and  $\sim 4$   $\mu\text{m}$ , respectively. While these detectors could operate at much higher temperatures than InSb-based MWIR detectors, their

(Received December 2, 2018; accepted April 24, 2019; published online May 3, 2019)

spectral responses do not cover the full ( $3\ \mu\text{m}$  to  $5\ \mu\text{m}$ ) MWIR atmospheric transmission window. This motivated us to develop *nBn*-architecture-compatible detectors with cutoff wavelength longer than  $5\ \mu\text{m}$ . We started out in 2008 by reproducing the standard  $4\text{-}\mu\text{m}$ -cutoff *nBn* based on the design by Maimon and Wicks,<sup>3</sup> using  $\text{InAs}_{0.91}\text{Sb}_{0.09}$  absorber lattice matched to GaSb substrate and an AlAsSb electron unipolar barrier. Our work with the bulk InAsSb *nBn* continued with follow-on studies of their high-temperature behavior,<sup>4</sup> as well as microlens-enhanced devices.<sup>5</sup> After demonstrating good material quality and device performance with the standard design, we started work on extending the cutoff wavelength to longer than  $4\ \mu\text{m}$ , with the goal of reaching beyond  $5\ \mu\text{m}$ . In designing an extended-cutoff absorber for lattice-matched or pseudomorphic growth on GaSb substrate, we have at our disposal GaAsSb, GaInSb, InGaAs, and InAsSb, all of which can have lattice constants relatively close to that of the GaSb substrate. For simplicity, however, we use only InAsSb. More specifically, we use combinations of InAs, InAsSb, and InSb (Fig. 1a). Since this approach does not use gallium (i.e., is “Ga free”), it simplifies material growth. Between 2008 and 2010, we examined a variety of absorbers based on the combination of InAs, InAsSb, and InSb, including

bulk InAsSb, InSb quantum dot layers embedded in InAsSb matrix, InSb/InAsSb superlattice, InSb/InAs superlattice, and finally InAs/InAsSb superlattice (see illustrations in Fig. 1). Below we briefly describe these developments.

In 2008, we started with standard Maimon and Wicks *nBn* structures using InAsSb absorbers approximately lattice-matched to the GaSb substrate (i.e., InAsSb with  $\sim 8.5\%$  Sb). Figure 2a shows the spectral response of two such devices, with cutoff length of  $4.0\ \mu\text{m}$  and  $4.1\ \mu\text{m}$ . Later, in 2008, we demonstrated our first extended-cutoff device. We had been working on quantum dot infrared photodetectors (QDIPs),<sup>6,7</sup> so we turned to quantum dots (QDs) for a possible solution. Our structure contains a simple modification of the standard  $4\text{-}\mu\text{m}$ -cutoff *nBn* design. We took this structure and periodically inserted InSb QD layers into the InAsSb absorber matrix. The QDs are formed by a self-assembly process when an approximately  $8\text{-}\text{\AA}$ -thick layer (exceeding the critical thickness) of InSb is deposited; the QD layers are separated by spacing of 80 monolayers of  $\text{InAs}_{0.92}\text{Sb}_{0.08}$ . The Sb fraction in the InAsSb matrix is reduced slightly from the standard *nBn* design in order to achieve better overall strain balancing against the insertion of InSb QDs (InSb has a larger lattice constant than the GaSb substrate). Figure 2b

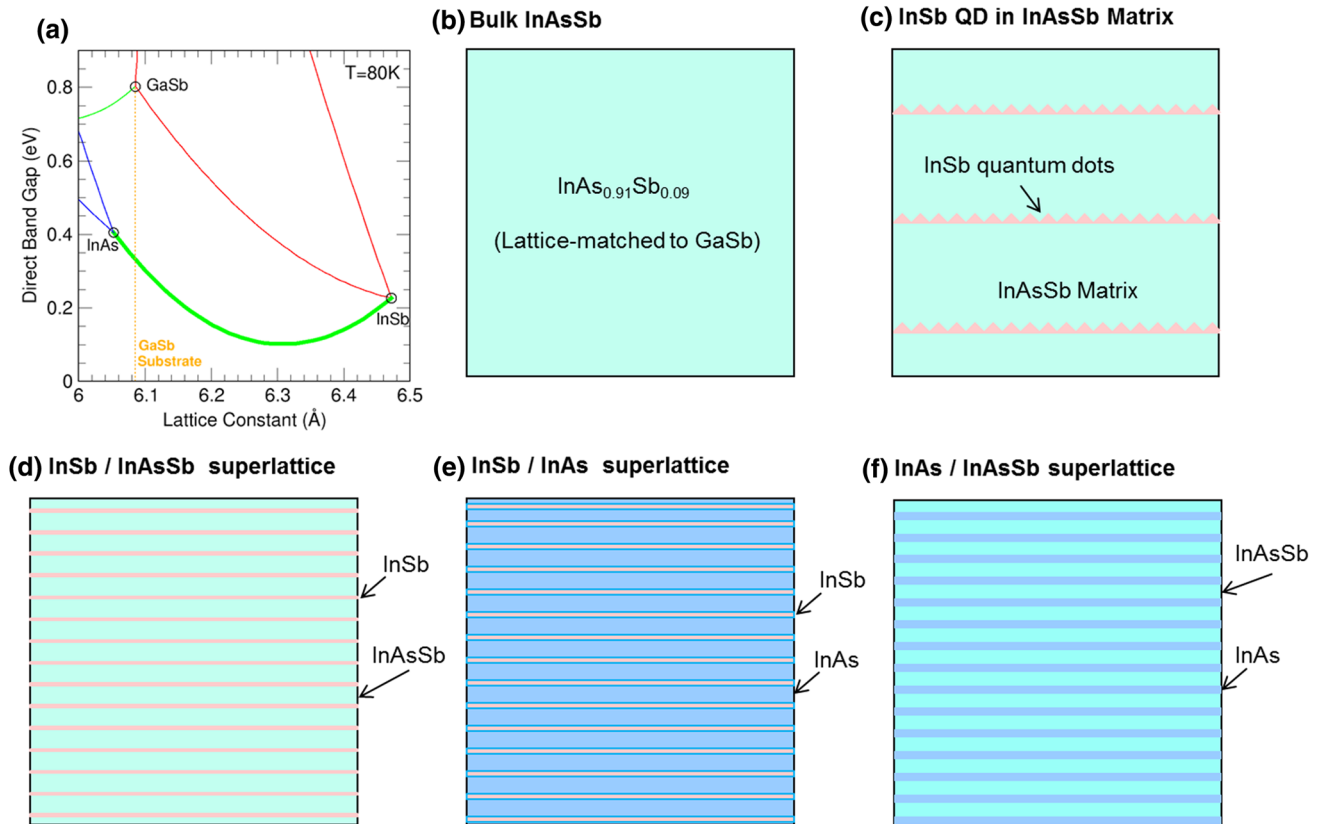


Fig. 1. (a) Direct bandgap versus lattice constant for InAsSb and related III-V semiconductors. (b–f) Schematic illustrations of InAs-, InAsSb-, and InSb-based infrared materials used in development of mid-wavelength *nBn* detectors.

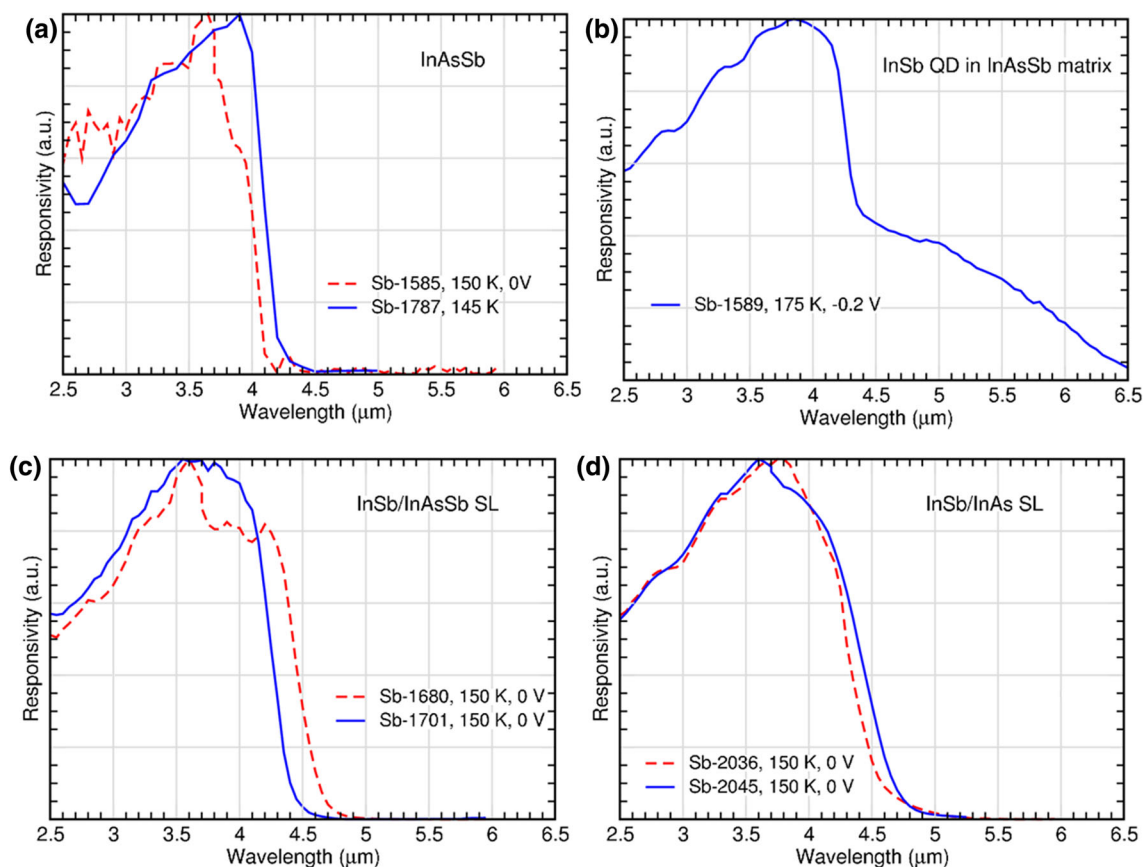


Fig. 2. Spectral responsivity for  $nBn$  devices with the following absorbers: (a) bulk InAsSb, (b) InSb quantum dots embedded in InAsSb matrix, (c) InSb/InAsSb superlattice, and (d) InSb/InAs superlattice. See text for InAsSb composition.

shows the spectral response of such a device, which appears to have an extended response past  $5.5 \mu\text{m}$ . However, a noticeable reduction in photoresponse is found for wavelengths greater than the InAsSb matrix cutoff wavelength ( $\sim 4.1 \mu\text{m}$ ).<sup>8,9</sup> Basically, the response below  $4.1 \mu\text{m}$  is due to the InAsSb matrix, while the longer wavelength response is due to the (type II) transition between the InSb QD valence band and InAsSb conduction band.

To remove the bimodal behavior found in the quantum dot barrier photodetectors, in 2008 to 2009 we reduced the InSb layer thickness from  $\sim 8 \text{ \AA}$  to  $\sim 3 \text{ \AA}$  to  $5 \text{ \AA}$ . The InSb layers periodically inserted into the InAsSb matrix are kept thin enough so that they form coherently strained planar layers rather than quantum dot layers. In this way, we effectively have a digital alloy, or an InSb/InAsSb type II superlattice.<sup>10</sup> The typical absorber superlattice period contains 1 monolayer of InSb and 15 monolayers of InAsSb. The Sb fraction in InAsSb is kept at lower than that in the lattice-matched InAsSb alloy to balance the compressive strain from the InSb layers. The advantage of this approach is that, compared with a bulk InAsSb alloy having the same net InSb content, the InAsSb/InSb digital alloy has a smaller bandgap (hence longer cutoff wavelength).

Using this approach, we made a number of devices, with cutoff wavelength ranging from  $4.1 \mu\text{m}$  to  $4.5 \mu\text{m}$ . Figure 2c shows the spectral response from two such samples. In sample Sb-1680, each period of the superlattice contains  $46 \text{ \AA}$  of  $\text{InAs}_{0.93}\text{Sb}_{0.07}$  and  $3 \text{ \AA}$  of InSb, and in sample Sb-1701,  $84 \text{ \AA}$  of  $\text{InAs}_{0.935}\text{Sb}_{0.065}$  and  $3 \text{ \AA}$  of InSb. Although we were able to extend the cutoff wavelength to beyond the  $4.2\text{-}\mu\text{m}$   $\text{CO}_2$  absorption line, we were not able to incorporate enough InSb in the absorber to reach  $5 \mu\text{m}$  cutoff.<sup>11</sup> A demonstration FPA showed  $4.8 \mu\text{m}$  cutoff, yielding reasonable imagery at an operating temperature of  $140 \text{ K}$ , although the detector material appeared to be highly strained due to the higher net InSb content. The difficulty in reaching  $> 5 \mu\text{m}$  cutoff with this approach is the limited InSb layer thickness. In general, the net InSb content in the coherently strained InAsSb/InSb digital alloy is less than the InSb/InAsSb embedded quantum dot material.

Early in 2010, we replaced the InAsSb layers with InAs to form InSb/InAs superlattices. This is to take advantage of the fact that (when grown on GaSb substrate) the InAs layers are more tensile than InAsSb, and offer more leverage in strain balancing the highly compressive InSb layers. The typical

absorber superlattice period contains 1.5 monolayers of InSb and 13 monolayers of InAs. Using this approach, we made a number of devices, with cutoff wavelength ranging from  $4.1\ \mu\text{m}$  to  $4.8\ \mu\text{m}$ . Figure 2d shows the spectral response from two of the samples. We found that, although we are able to use thicker InSb layers than in the InSb/InAsSb superlattices, we still could not reach  $> 5\ \mu\text{m}$  cutoff.

The challenge for the InSb/InAs superlattice is basically the same as in the case of the InSb/InAsSb superlattice. The difficulty in both cases is that the InSb layer thickness needs to be kept below the critical thickness ( $\sim 2$  monolayers). From strain-balancing considerations, this in turn keeps the InAs or InAsSb layer thicknesses relatively thin. In superlattices where both the InSb and the InAs (or InAsSb) layers are thin, the valence- and conduction-band quantization energies are high, thus the superlattice bandgap cannot be made sufficiently small. To achieve longer than  $5\ \mu\text{m}$  cutoff, we need to use superlattices that allow for longer periods.

Later in 2010, we replaced the InSb layers in the InAs/InSb superlattice by InAsSb. This is the remaining choice out of the three possible bilayer superlattices that can be made from InAs, InAsSb, and InSb (i.e., InAsSb/InSb, InAs/InSb, and InAs/InAsSb superlattices). The InAs/InAsSb superlattices are also grown on GaSb substrates, and use compressive InAsSb layers (with  $> 8\%$  InSb content; typically ranging from 20% to 50%) to strain balance against the tensile InAs layers. This is in contrast to the InAsSb/InSb structure, where the InAsSb layers have  $< 8\%$  InSb content, and have tensile strain. In the cases of InAsSb/InSb and InAs/InSb superlattices, the InSb layers are very highly strained, with critical thickness of less than two monolayers. In the InAs/InAsSb superlattices, the InAsSb layers are much less strained, and can be much thicker. With the InAs/InAsSb absorber, we were finally able to achieve  $> 5\ \mu\text{m}$  cutoff wavelength in July 2010.

Among the first InAs/InAsSb  $nBn$  samples grown was Sb-2082. The  $n$ -type top contact and the  $n$ -type absorber are made from the same superlattice, where each period consists nominally of  $48\ \text{\AA}$  of InAs and  $13\ \text{\AA}$  of  $\text{InAs}_{0.45}\text{Sb}_{0.55}$ . The absorber consists of a 400-period superlattice with  $n \sim 1.5 \times 10^{16}\ \text{cm}^{-3}$  doping, and the top contact consists of 12 periods with  $n \sim 1.5 \times 10^{16}\ \text{cm}^{-3}$  doping capped by another 6 periods with  $n \sim 1 \times 10^{17}\ \text{cm}^{-3}$  doping. The electron unipolar barrier consists of  $1000\ \text{\AA}$  of  $\text{Al}_{0.88}\text{Ga}_{0.12}\text{Sb}$  doped at  $p \sim 1.5 \times 10^{15}\ \text{cm}^{-3}$ . Sb-2082 has a 77-K minority-carrier lifetime of 282 ns, which is relatively short compared with more recent samples; a subsequent not-intentionally doped MWIR sample demonstrated a much longer minority-carrier lifetime of  $1.8\ \mu\text{s}$ , with Shockley–Read–Hall (SRH) lifetime of  $10\ \mu\text{s}$ .<sup>12</sup> Figure 3 shows the 150-K photoluminescence spectrum with a peak at  $5.25\ \mu\text{m}$ ; it also shows the 77-K, 150-K, and 200-K spectral response with approximate cutoff at  $5.1\ \mu\text{m}$ ,  $5.3\ \mu\text{m}$ , and  $5.6\ \mu\text{m}$ , respectively. Figure 4

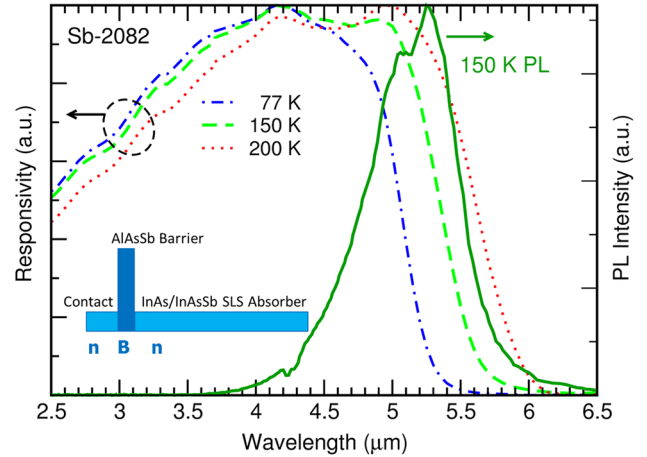


Fig. 3. Spectral responsivity and photoluminescence spectrum for  $nBn$  device with InAs/InAsSb type II strained-layer superlattice absorbers from sample Sb-2082. Inset shows a schematic energy band diagram of the device.

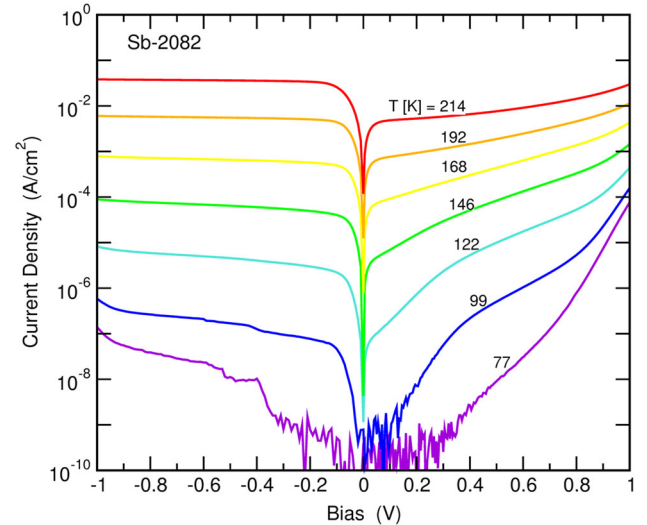


Fig. 4. Dark current density–voltage characteristics at temperatures ranging from 77 K to 214 K.

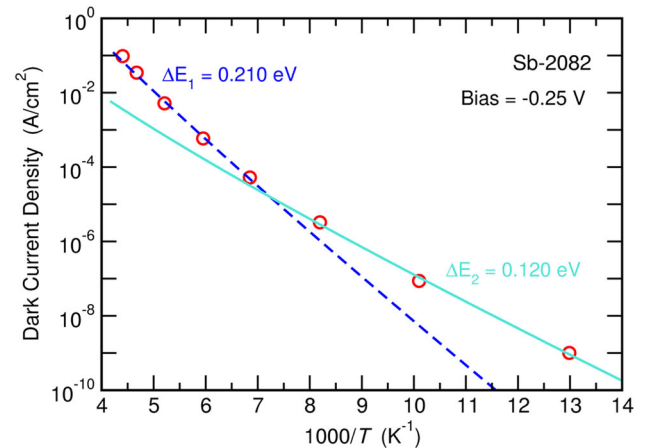


Fig. 5. Arrhenius analysis plot for a device from sample Sb-2082.





Fig. 6. FPA images ( $320 \times 256$ ) at 150 K from two different MWIR InAs/InAsSb superlattice  $nBn$  samples.

shows the dark current density–voltage curves at various temperatures. The estimated dark current density at 150 K is  $\sim 8 \times 10^{-5}$  A/cm<sup>2</sup>, which is approximately 14 times that given by Rule 07<sup>13</sup> for a 5.3- $\mu$ m-cutoff devices. The Arrhenius analysis in Fig. 5 shows that, at above 140 K, the activation energy is  $\sim 210$  meV, which is fairly close to the bandgap derived from the cutoff wavelength, indicating near-diffusion-limited behavior. From 140 K down to 77 K, the activation energy is  $\sim 120$  meV, indicating G–R dark current dominance. The diffusion/G–R dark current crossover of 140 K in this early sample is high compared with more recent MWIR samples.<sup>1,14</sup>

Figure 6 shows 150-K images taken with proof-of-concept FPAs made from InAs/InAsSb superlattice  $nBn$  samples in 2011. Detector arrays were hybridized to the 30- $\mu$ m pitch,  $320 \times 256$  format ISC-9705 readout integrated circuit (ROIC). With these prototype FPAs, there was no epoxy underfill and the substrate was not removed. FPAs 11NRA01 and 11NRA04 were fabricated from samples Sb-2083 and Sb-2157, respectively, with 150-K cutoff wavelength of 5.1  $\mu$ m and 5.4  $\mu$ m. These preliminary FPA results were encouraging in that we were able to reach  $> 5$   $\mu$ m cutoff wavelength while operating at significantly higher temperature than InSb. Continued improvement led to much better FPA performance by 2012.<sup>1,2</sup>

We were able to make fairly rapid progress because, in general, the InAs/InAsSb superlattice is easier to grow than the InAs/GaSb superlattice, and appears to have better defect tolerance. Molecular beam epitaxy (MBE) growth of the InAs/InAsSb superlattice in principle involves only turning on and off the Sb shutter, in contrast to the use of four shutters required to grow the InAs/GaSb superlattice.<sup>1,15</sup> The typical (nearly) strain-balanced InAs/InAsSb superlattice is  $\sim 90\%$  net InAs. The conduction-band edge of InAs is low compared with other III–V semiconductors, and many of the defect energy levels in InAs tend to be in resonance with the conduction band, rather than in the bandgap

where they are detrimental. The InAs/InAsSb superlattices also have very low conduction edges, which are similarly beneficial for defect tolerance. Anecdotally, Sb-2083 was grown on a vintage  $\sim 2011$  experimental 4-inch-diameter GaSb substrate. At that time, the 4-inch substrate surface polishing was not nearly as mature as it is today. The fact that we were nevertheless able to obtain reasonable FPA results can be attributed in part to the defect tolerance of the InAs/InAsSb superlattice (the  $nBn$  device architecture being another major contributing factor).

Some of our initial results on the InAs/InAsSb T2SLS detector and FPA were briefly mentioned in a patent disclosure<sup>15</sup> that describes the concept of building unipolar barrier infrared detectors using superlattice absorbers constructed from InAs, InGaAs, and InAsSb. Meanwhile, the report of significantly longer minority-carrier lifetimes in long-wavelength infrared (LWIR) InAs/InAsSb SLS than InAs/GaSb SL<sup>16</sup> generated growing interest in the InAs/InAsSb SLS as an infrared detector absorber. Soon after, the Zhang group demonstrated an InAs/InAsSb SLS LWIR photodetector<sup>17</sup> based on the  $nBn$  device design. The Razeghi group provided further impetus by showing the versatility of the InAs/InAsSb SLS, having reported MWIR,<sup>18</sup> LWIR,<sup>19–21</sup> very long-wavelength infrared (VLWIR),<sup>22</sup> and bias-selectable dual-band MWIR/LWIR infrared photodetectors.<sup>23</sup> Results on InAs/InAsSb SLS detectors have also been reported by many other research groups worldwide.<sup>24–27</sup>

## DISCUSSION AND CONCLUSIONS

We have described the development at NASA JPL leading to MWIR InAs/InAsSb T2SLS unipolar barrier detectors and FPAs that have demonstrated much higher operating temperatures than InSb, a major incumbent MWIR FPA technology. The InAs/InAsSb T2SLS has a much longer SRH lifetime compared with InSb. The standard ion-implanted planar InSb detector is limited by the relatively

short SRH lifetime ( $\sim 300$  ns), and is depletion current dominated at below 125 K.<sup>28</sup> The MWIR InAs/InAsSb T2SLS absorber, typically not intentionally doped, has demonstrated SRH lifetime of  $\sim 10$   $\mu$ s,<sup>12,29</sup> and the detector also benefits from depletion dark current reduction afforded by the  $nBn$  architecture. Use of a unipolar barrier architecture such as  $nBn$  is crucial for the InAs/InAsSb T2SLS, which, like InAs, always has a degenerate  $n$ -type surface regardless of doping type. Without adequate surface passivation, an InAs/InAsSb T2SLS  $p$ - $n$  homojunction would be dominated by surface leakage dark current due to the surface shunt. The  $nBn$  device structure also serves to reduce the depletion dark current found in a  $p$ - $n$  homojunction.

Compared with MCT, the InAs/InAsSb T2SLS has the benefit of III-V robustness advantages for manufacturing like InSb. However, MCT has two notable advantages. MCT has very long SRH lifetime that enables the fully depleted device architecture for high-operating-temperature (HOT) operation.<sup>30,31</sup> MCT also benefits from wide-band-gap diffused CdTe surface passivation. For  $n$ -type InAs/InAsSb T2SLS, the degenerate  $n$ -type surface is benign, since it repels minority carriers. However, for  $p$ -type InAs/InAsSb T2SLS, the degenerate  $n$ -type surface is problematic; the challenge of developing effective passivation schemes needs to be met.

It is also interesting to compare the InAs/InAsSb T2SLS with the more established InAs/GaSb type II superlattice (T2SL). The InAs/InAsSb T2SLS is easier to grow,<sup>15</sup> is more defect tolerant, and has longer minority-carrier lifetime.<sup>16</sup> On the other hand, it covers a somewhat smaller adjustable cutoff wavelength range ( $\sim 4$   $\mu$ m to beyond 14  $\mu$ m), and has weaker optical absorption<sup>32,33</sup> and more challenging vertical hole transport,<sup>34</sup> especially in the long-wavelength infrared (LWIR). Good detector and FPA results have been demonstrated with both InAs/GaSb T2SL and InAs/InAsSb T2SLS; the InAs/InAsSb T2SLS can be highly effective when implemented in the MWIR.

## ACKNOWLEDGMENTS

The authors thank J. Nguyen, J. M. Mumolo, J. K. Liu, and A. Liao for technical assistance. The research described in this publication was carried out at the Jet Propulsion Laboratory, California Institute of Technology, under a contract with the National Aeronautics and Space Administration.

## REFERENCES

1. D.Z. Ting, A. Soibel, A. Khoshakhlagh, S.B. Rafol, S.A. Keo, L. Höglund, A.M. Fisher, E.M. Luong, and S.D. Gunapala, *Appl. Phys. Lett.* 113, 021101 (2018).
2. D.Z. Ting, S.B. Rafol, K.A. Sam, J. Nguyen, A. Khoshakhlagh, A. Soibel, L. Höglund, A.M. Fisher, E.M. Luong, J.M. Mumolo, J.K. Liu, and S.D. Gunapala, *IEEE Photon. J.* 10, 6804106 (2018).
3. S. Maimon and G.W. Wicks, *Appl. Phys. Lett.* 89, 151109 (2006).
4. A. Soibel, C.J. Hill, S.A. Keo, L. Höglund, R. Rosenberg, R. Kowalczyk, A. Khoshakhlagh, A. Fisher, D.Z.-Y. Ting, and S.D. Gunapala, *Appl. Phys. Lett.* 105, 023512 (2014).
5. A. Soibel, S.A. Keo, A. Fisher, C.J. Hill, E. Luong, D.Z. Ting, S.D. Gunapala, D. Lubyshev, Y. Qiu, J.M. Fastenau, and A.W.K. Liu, *Appl. Phys. Lett.* 112, 041105 (2018).
6. D.Z.-Y. Ting, S.V. Bandara, S.D. Gunapala, J.M. Mumolo, S.A. Keo, C.J. Hill, J.K. Liu, E.R. Blazejewski, S.B. Rafol, and Y.-C. Chang, *Appl. Phys. Lett.* 94, 111107 (2009).
7. S.D. Gunapala, S.V. Bandara, C.J. Hill, D.Z. Ting, J.K. Liu, S.B. Rafol, E.R. Blazejewski, J.M. Mumolo, S.A. Keo, S. Krishna, Y.-C. Chang, and C.A. Shott, *IEEE J. Quantum Electron.* 43, 230 (2007).
8. C.J. Hill, A. Soibel, S.A. Keo, J.M. Mumolo, D.Z. Ting, and S.D. Gunapala, *Electron. Lett.* 46, 1286 (2010).
9. D.Z.-Y. Ting, A. Soibel, S.A. Keo, A. Khoshakhlagh, C.J. Hill, L. Höglund, J.M. Mumolo, and S.D. Gunapala, *J. Electron. Mater.* 42, 3071 (2013).
10. C.J. Hill, D.Z. Ting, and S.D. Gunapala, U.S. Patent Application 2010/0155777 (2010); U.S. patent 9,466,741 (2016).
11. A. Soibel, D.Z. Ting, C.J. Hill, A.M. Fisher, L. Höglund, S.A. Keo, and S.D. Gunapala, *Appl. Phys. Lett.* 109, 103505 (2016).
12. L. Höglund, D.Z. Ting, A. Khoshakhlagh, A. Soibel, C.J. Hill, A. Fisher, S. Keo, and S.D. Gunapala, *Appl. Phys. Lett.* 103, 221908 (2013).
13. W.E. Tennant, *J. Electron. Mater.* 39, 1030 (2010).
14. D.Z. Ting, A. Soibel, A. Khoshakhlagh, S.A. Keo, S.B. Rafol, A.M. Fisher, B.J. Pepper, E.M. Luong, C.J. Hill, and S.D. Gunapala, *SPIE Proceedings Volume 10624, Infrared Technology and Applications XLIV*; 1062410 (2018).
15. D.Z. Ting, A. Khoshakhlagh, A. Soibel, C.J. Hill, and S.D. Gunapala, U.S. Patent Application 13/197,588 (2011); U.S. Patent 8,217,480 (2012).
16. E.H. Steenbergen, B.C. Connelly, G.D. Metcalfe, H. Shen, M. Wraback, D. Lubyshev, Y. Qiu, J.M. Fastenau, A.W.K. Liu, S. Elhamri, O.O. Cellek, and Y.-H. Zhang, *Appl. Phys. Lett.* 99, 251110 (2011).
17. H.S. Kim, O.O. Cellek, Z.-Y. Lin, Z.-Y. He, X.-H. Zhao, S. Liu, H. Li, and Y.-H. Zhang, *Appl. Phys. Lett.* 101, 161114 (2012).
18. D. Wu, Q. Durlin, A. Dehzangi, Y. Zhang, and M. Razeghi, *Appl. Phys. Lett.* 114, 011104 (2019).
19. A. Haddadi, G. Chen, R. Chevallier, A.M. Hoang, and M. Razeghi, *Appl. Phys. Lett.* 105, 121104 (2014).
20. A. Haddadi, A. Dehzangi, S. Adhikary, R. Chevallier, and M. Razeghi, *APL Mater.* 5, 035502 (2017).
21. R. Chevallier, A. Haddadi, and M. Razeghi, *Nat. Sci. Rep.* 7, 12617 (2017).
22. A.M. Hoang, G. Chen, R. Chevallier, A. Haddadi, and M. Razeghi, *Appl. Phys. Lett.* 104, 251105 (2014).
23. A. Haddadi, R. Chevallier, G. Chen, A.M. Hoang, and M. Razeghi, *Appl. Phys. Lett.* 106, 011104 (2015).
24. E.A. Plis, T. Schuler-Sandy, D.A. Ramirez, S. Myers, and S. Krishna, *Electron. Lett.* 51, 2009 (2015).
25. R. Hao, Y. Ren, S. Liu, J. Guo, G. Wang, Y. Xu, and Z. Niu, *J. Cryst. Growth* 470, 33 (2017).
26. K. Michalczewski, L. Kubiszyn, P. Martyniuk, C.H. Wu, J. Jureńczyk, K. Grodecki, D. Benyahia, A. Rogalski, and J. Piotrowski, *Infrared Phys. Technol.* 95, 222 (2018).
27. D.J.P. Perez, L. Cerutti, J.B. Rodriguez, T. Cerba, T. Baron, E. Tournié, and P. Christol, *Infrared Phys. Technol.* 96, 39 (2019).
28. M.A. Kinch, *Fundamentals of Infrared Detector Materials* (Bellingham: SPIE Press, 2007), p. 57.

29. B.V. Olson, E.A. Shaner, J.K. Kim, J.F. Klem, S.D. Hawkins, L.M. Murray, J.P. Prineas, M.E. Flatte, and T.F. Boggess, *Appl. Phys. Lett.* 101, 092109 (2012).
30. T. Ashley and C.T. Elliot, *Electron. Lett.* 21, 451 (1985).
31. D. Lee, M. Carmody, E. Piquette, P. Dreiske, A. Chen, A. Yulius, D. Edwall, S. Bhargava, M. Zandian, and W.E. Tennant, *J. Electron. Mater.* 45, 4587 (2016).
32. P.C. Klipstein, Y. Livneh, A. Glozman, S. Grossman, O. Klin, N. Snapi, and E. Weiss, *J. Electron. Mater.* 43, 2984 (2014).
33. I. Vurgaftman, G. Belenky, Y. Lin, D. Donetsky, L. Shterengas, G. Kipshidze, W.L. Sarney, and S.P. Svensson, *Appl. Phys. Lett.* 108, 222101 (2016).
34. D.Z. Ting, A. Soibel, and S.D. Gunapala, *Appl. Phys. Lett.* 108, 183504 (2016).

**Publisher's Note** Springer Nature remains neutral with regard to jurisdictional claims in published maps and institutional affiliations.